

1 **Supplementary Notes**

2 **Supplementary Note 1. Wind exposure metrics**

3 Sea-surface wind speed was obtained from the NOAA blended sea-surface wind product
4 (Wallcraft et al. 2009), a global 0.25° latitude–longitude analysis that combines satellite
5 scatterometer and radiometer retrievals, buoy observations and numerical weather-prediction
6 output into monthly mean 10-m wind speed fields. For a bleaching observation at grid cell (i, j)
7 recorded in month M of year Y, the k-month antecedent mean wind speed (k = 6, 12) was computed
8 as the arithmetic mean of monthly wind speed over the k consecutive months ending in the survey
9 month:

$$10 \quad W_k(i,j) = (1/k) \sum_{n=0}^{k-1} W(Y-n, M-n, i, j).$$

11 The long-term background wind speed was computed as the mean of all N monthly fields
12 available for the cell over the 1993–2020 reference period:

$$13 \quad W_{LT}(i,j) = (1/N) \sum_{y=1993}^{2020} \sum_{m=1}^{12} W(y, m, i, j).$$

14 Antecedent windows capture transient wind forcing in the months preceding a survey, whereas
15 the long-term mean captures the persistent background regime that defines a site’s chronic
16 ventilation environment; the two are weakly correlated and were never entered in the same model.
17 Wind metrics were joined to bleaching records by exact match on grid-cell coordinates and, for the
18 antecedent windows, on survey month. The antecedent mean wind speed — the 6-month window
19 in the global dataset and the 12-month window in the in-situ dataset, each selected by AIC (ΔAIC
20 ≈ 20 favouring the 6-month window in the global dataset) — is the predictor entered in the models
21 and referred to as sustained wind in the main text. The long-term 1993–2020 mean is retained only
22 as a climatological reference; entered on its own it is not significantly associated with severity (odds
23 ratio ≈ 1.08 per s.d., $P = 0.36$), whereas the 6-month antecedent mean is strongly protective (odds
24 ratio ≈ 0.70 , $P < 10^{-6}$), indicating that the association operates on a seasonal-to-annual rather than
25 a decadal timescale.

26 **Supplementary Note 2. Tropical-cyclone power: reconstruction and** 27 **sensitivity**

28 Tropical-cyclone tracks were taken from IBTrACS v4.01 (Knapp et al. 2010), which provides
29 homogenized 6-hourly storm position, maximum sustained 10-m wind speed and central pressure
30 for all basins. For each reef location we retained every 6-hourly track point within a radius of 400
31 km. At each retained point the local wind speed $V(r)$ at radial distance r from the storm centre was
32 reconstructed with a Holland-type parametric profile (Holland 1980):

$$33 \quad V(r) = \sqrt{[B (\Delta P/\rho) (R_{max}/r)^B \exp(-(R_{max}/r)^B) + (r f / 2)^2] - r f / 2},$$

34 with central-pressure deficit $\Delta P = P_n - P_c$ (ambient $P_n = 1010$ hPa), radius of maximum wind
35 R_{max} , Holland shape parameter $B = 1.5$, air density $\rho = 1.15$ kg m⁻³ and Coriolis parameter $f = 2\Omega$
36 $\sin\phi$. When R_{max} or central pressure were missing from IBTrACS, R_{max} was set to 30 km and the
37 radial field scaled to the reported maximum sustained wind with exponential decay beyond R_{max} .
38 Tropical-cyclone power was accumulated as a power-dissipation–type quantity (Emanuel 2005), in
39 which the cube of wind speed gives intense storms a dominant weight:

40

$$TCPower = \sum_i V_i^3 \Delta t_i, \quad \Delta t_i = 6 \text{ h},$$

41

42

43

44

45

46

47

summed over all retained 6-hourly points within 400 km, over three windows: the 6 and 12 months preceding each observation, and cumulatively over 1993–2020 independent of survey date. Sensitivity tests varied the influence radius (200, 300, 400 km), the shape parameter B (1.3–1.8) and the default R_{\max} (20–40 km). Smaller radii and larger B reduced absolute TCPower but left the rank ordering of reef sites and the sign and significance of the TCPower–severity relationship unchanged; cumulative TCPower at reef sites therefore reflects storm frequency and intensity rather than the parametric assumptions of the reconstruction.

48

Supplementary Note 3. Box Upwelling–Diffusion (BUD) model

49

50

51

52

53

54

55

56

57

58

59

The wind– Ω relationship was interpreted with a steady-state Box Upwelling–Diffusion (BUD) model in the tradition of box-diffusion ocean–carbon models (Hoffert et al. 1981). A single well-mixed surface box — the mixed ocean layer (MOL) of thickness $h = 40$ m — exchanges dissolved inorganic carbon (DIC), total alkalinity (TA) and calcium with a fixed deep reservoir through wind-driven upwelling (velocity W) and vertical turbulent diffusion (eddy diffusivity A_z acting over thickness h), while exchanging CO_2 with the atmosphere (flux F_a) and removing carbon by biological export (B), partitioned between organic matter and CaCO_3 . The carbonate system, including aragonite saturation state Ω_{arag} , was evaluated from box TA and DIC with the seacarb package (Lavigne & Gattuso 2012) using the CO_2 solubility of Weiss (1974). Parameter values follow the reference implementation used to generate the results (Supplementary Code) and are listed in Supplementary Table 1.

60

Wind scaling.

61

62

Upwelling, diffusivity and biological export were each scaled to wind speed U relative to a reference trade-wind speed $U^* = 6 \text{ m s}^{-1}$ through independent power-law exponents m , q and n :

63

$$W(U) = W_0 (U/U^*)^m, \quad A_z(U) = A_{z0} (U/U^*)^q, \quad B(U) = B_0 (U/U^*)^n,$$

64

65

66

67

with the combined vertical exchange rate $M = W + A_z/h$. The air–sea CO_2 flux used a quadratic gas-transfer velocity $k = \alpha U^2$ (Wanninkhof 2014; Schmidt number 660), $F_a = \rho k K_0 (P_a - P_w)$, where P_a is atmospheric and P_w the box CO_2 partial pressure. Biological export was split as $F_{\text{org}} = -(1-r_{\text{CaCO}_3})B$ and $F_{\text{CaCO}_3} = -r_{\text{CaCO}_3} B$ (negative denoting removal from the MOL).

68

Steady-state balances.

69

70

Setting the surface-box tendencies to zero gives the MOL concentrations as deviations from the deep reservoir:

71

$$DIC_{\text{MOL}} = DIC_{\text{deep}} + (F_{\text{org}} + F_{\text{CaCO}_3} + F_a)/(\rho M),$$

72

73

$$TA_{\text{MOL}} = TA_{\text{deep}} + (2 F_{\text{CaCO}_3} + r_{\text{N}} F_{\text{org}^{\text{prod}}})/(\rho M), \quad Ca_{\text{MOL}} = Ca_{\text{deep}} + F_{\text{CaCO}_3}/(\rho M),$$

74

75

76

where $r_{\text{N}} = 16/106$ is the nitrate-to-carbon alkalinity contribution of organic production. Because F_a itself depends on P_w , the box $p\text{CO}_2$ was solved self-consistently for each U (root-finding on the residual between the carbonate-system $p\text{CO}_2$ and the assumed P_w), after which

77 Ω_{arag} was returned by seacarb. Carbon-budget closure ($F_a + F_{\text{up}} + F_d - B \approx 0$) was confirmed at
78 every solution.

79 ***Parameter grid and the three reported cases.***

80 The model was run for $U = 1\text{--}10 \text{ m s}^{-1}$ over the full grid $m, n, q \in \{0, 1, 2\}$ (27 combinations).
81 For the main-text figure we report three cases that bracket the plausible coupling of the surface
82 carbon budget to wind while holding diffusivity wind-independent ($q = 0$), the latter justified by
83 the limited variability of turbulent diffusion across the Pacific pycnocline (Itoh et al. 2021): (i) m
84 $= n = q = 0$, in which neither upwelling nor productivity responds to wind; (ii) $m = n = 1, q = 0$;
85 and (iii) $m = n = 2, q = 0$, the last corresponding to an Ekman-type response in which wind-driven
86 transport scales with wind stress (U^2). We set $n = m$ because, in the open ocean, biological export
87 is supplied largely by upwelled nutrients, so productivity and upwelling are expected to co-vary;
88 the cases $n = m = 0$ and $n = m = 2$ then bracket the realistic intermediate behaviour, and $q = 0$
89 isolates the role of advective/productive coupling from diffusive change.

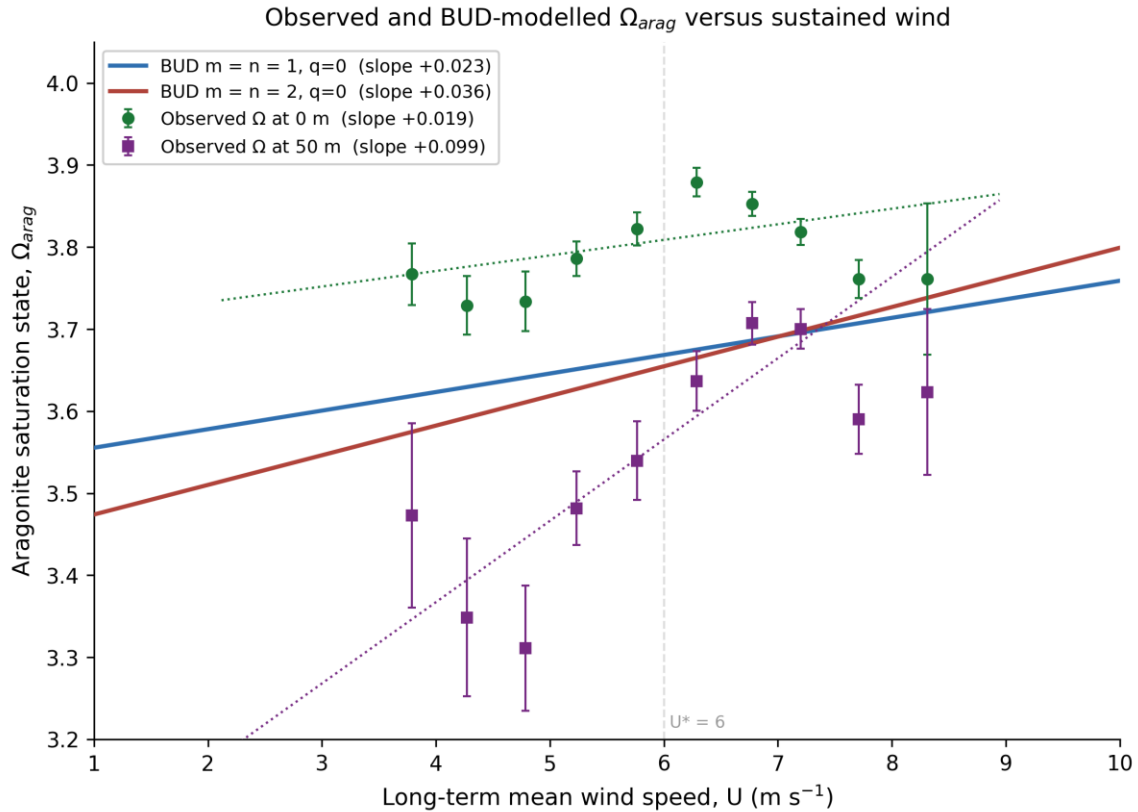
90 ***Result and comparison with observations.***

91 Across these cases the modelled steady-state dependence of surface Ω_{arag} on wind speed rises
92 from essentially flat (slightly negative, $-0.001 \text{ per m s}^{-1}$) at $m = n = 0$ to weakly positive at $m = n$
93 $= 1$ ($+0.028 \text{ per m s}^{-1}$) and $m = n = 2$ ($+0.042 \text{ per m s}^{-1}$). In no case does the model produce the
94 strong negative Ω –wind relationship that would be expected if wind simply upwelled carbon-rich,
95 low- Ω water; instead, the wind-driven increase in both CO_2 outgassing capacity and biological
96 drawdown offsets the upwelling supply of DIC, leaving a weak positive net dependence. This
97 reproduces the sign and approximate magnitude of the observed relationship. In the reef
98 observations the Ω –wind slope is $+0.019 \text{ per m s}^{-1}$ at the surface (0 m; Pearson $r = +0.15$) and
99 $+0.099 \text{ per m s}^{-1}$ at 50 m ($r = +0.38$). The modelled slope ($+0.03$ to $+0.04$) lies between these and
100 is closer to the subsurface value, as expected because the BUD box represents an integrated mixed
101 ocean layer rather than the skin surface; tropical mixed-layer depth is typically $\sim 30\text{--}50 \text{ m}$ (de Boyer
102 Montégut et al. 2004), so the 50-m observations are the more appropriate comparison and there the
103 positive relationship is clearest. We emphasize that the aragonite-saturation fields are gridded at
104 $\sim 1^\circ$ ($\sim 100 \text{ km}$), coarser than the 0.25° wind product, so the wind– Ω relationship is treated as a long-
105 term climatological association rather than an event-scale one; this resolution mismatch, together
106 with the use of fixed deep-reservoir end-members, is the main source of quantitative uncertainty in
107 the comparison. Finer-scale carbonate-chemistry products, as they become available, could test this
108 wind– Ω association at reef-relevant scales.

109 ***Supplementary Table 1. BUD model constants (reference implementation).***

Symbol	Value	Meaning
ρ	1025 kg m^{-3}	seawater density
h	40 m	mixed ocean layer (MOL) thickness
S, T	35, 25 °C	salinity, temperature
TA_deep	$2350 \mu\text{mol kg}^{-1}$	deep total alkalinity
DIC_deep	$2100 \mu\text{mol kg}^{-1}$	deep dissolved inorganic carbon
Ca_deep	$10.3 \text{ mmol kg}^{-1}$	deep calcium

U^*	6 m s^{-1}	reference (trade-wind) speed
W_0	$4.7 \times 10^{-7} \text{ m s}^{-1}$	upwelling velocity at U^*
A_{z0}	$1 \times 10^{-5} \text{ m}^2 \text{ s}^{-1}$	vertical eddy diffusivity at U^*
B_0	$32.4 \times 10^{-9} \text{ mol C m}^{-2} \text{ s}^{-1}$	biological export at U^*
r_{CaCO_3}	0.07	CaCO_3 fraction of export
r_{N}	16/106	nitrate alkalinity per organic C
α	$6.97 \times 10^{-7} \text{ m s}^{-1} \text{ per } U^2$	gas-transfer coefficient (Wanninkhof 2014)
P_a	430 μatm	atmospheric $p\text{CO}_2$
K_0	$2.85 \times 10^{-2} \text{ mol kg}^{-1} \text{ atm}^{-1}$	CO_2 solubility (Weiss 1974)



110

111 **Supplementary Figure 1. Observed and BUD-modelled aragonite saturation state**
 112 **(Ω_{arag}) versus sustained background wind.** Observed Ω_{arag} at 0 m (green circles) and
 113 50 m (purple squares), from an observation-based gridded product, binned by long-term
 114 mean wind speed (0.5 m s^{-1} bins, $2\text{--}9 \text{ m s}^{-1}$; mean \pm 95% confidence interval) with least-
 115 squares fits (dotted). Both depths show a weak positive Ω -wind relationship, stronger at
 116 50 m (slope $+0.099 \text{ per m s}^{-1}$) than at the surface ($+0.019 \text{ per m s}^{-1}$). Solid lines are linear
 117 fits to the steady-state Box Upwelling-Diffusion (BUD) model (Supplementary Note 3) for
 118 the two physically plausible wind-coupling cases: upwelling and productivity scaling
 119 linearly ($m = n = 1$; blue) and quadratically ($m = n = 2$; red) with wind, vertical diffusivity
 120 held wind-independent ($q = 0$; Itoh et al. 2021). The model reproduces the weak positive
 121 sensitivity of Ω to wind and excludes the strong negative relationship expected if wind-
 122 driven upwelling of carbon-rich, low- Ω water dominated; the $m = n = 2$ slope ($+0.036 \text{ per}$
 123 m s^{-1}) best matches the data. Because the BUD box represents an integrated mixed ocean

124 layer (~30–50 m; de Boyer Montégut et al. 2004), the modelled curves fall between the 0 m
125 and 50 m observations.

126 **Supplementary Note 4. Shapley decomposition of explained variation**

127 To attribute McFadden’s pseudo- R^2 among predictor groups while respecting within-group
128 collinearity, we used a Shapley decomposition (Shapley 1953; Grömping 2007) at the level of
129 predictor groups rather than individual coefficients. McFadden’s pseudo- R^2 (McFadden 1974) for
130 a fitted ordinal model is $R^2 = 1 - \ell(\text{model})/\ell(\text{null})$, with ℓ the maximized log-likelihood and the
131 null model containing only the cumulative-logit thresholds. For G mutually exclusive groups, the
132 Shapley value of group g is its average marginal contribution to R^2 over all orderings of the groups:

$$133 \quad \varphi_g = \sum_{\{S \subseteq G \setminus \{g\}\}} [|S|! / (|G| - |S| - 1)! / |G|!] [R^2(S \cup \{g\}) - R^2(S)].$$

134 With at most four groups the 2^G subset models were enumerated and fitted exactly, so no
135 Monte-Carlo sampling was required; the resulting Shapley values are additive and sum to the full-
136 model R^2 , and the decomposition is order-independent. Groups were: for the global dataset,
137 Thermal (degree-heating weeks and the three SST principal components), Wind (6-month
138 antecedent mean wind), Cyclone (cumulative tropical-cyclone power) and Other site descriptors
139 (distance to shore, turbidity and exposure); for the in-situ dataset, Thermal (degree-heating weeks,
140 diurnal temperature range, rate of temperature change, acute stress and thermal trajectory), Depth
141 and Wind. Uncertainty in each group’s share was obtained by bootstrap resampling of grid cells for
142 the global dataset. For the within-region variant, marine-realm indicators (Spalding et al. 2007)
143 were included in the null model and in every subset model, so that the decomposition partitions
144 only the deviance explained beyond region; this confirmed that the wind share is not inflated by
145 between-region structure. The within-region estimators themselves (realm fixed effects and the
146 Mundlak within–between decomposition; Mundlak 1978; Bell & Jones 2015) are described in the
147 main-text Methods.

148 **Supplementary Note 5. Boundary-layer scaling of ROS clearance**

149 This note supports the mechanistic interpretation presented in the Discussion and Fig. 5. It is
150 intended as a scaling argument rather than a fitted component of the statistical analysis and should
151 therefore be viewed as a leading hypothesis consistent with the data and with controlled flow
152 experiments, rather than as a mechanism demonstrated directly by the present study. Direct field
153 evidence linking sustained background wind, as distinct from local waves and currents, to diffusive-
154 boundary-layer thickness and reactive-oxygen-species (ROS) efflux at bleaching-relevant scales
155 remains limited.

156 Export of reactive oxygen species (for example, H_2O_2) from coral tissue to the overlying water
157 is constrained by molecular diffusion across the diffusive boundary layer (DBL). The diffusive flux
158 is

159

$$160 \quad J = k (C_t - C_\infty), \quad k = D/\delta,$$

161 where C_t and C_∞ are tissue-surface and free-stream concentrations, k is the mass-transfer
162 coefficient, D the molecular diffusivity and δ the DBL thickness. Mass transfer over the colony is

163 described by the Sherwood number $Sh = kL/D$, related to flow through $Sh = a \cdot Re^m \cdot Sc^n$, with
164 Reynolds number $Re = U_{\text{flow}} L/\nu$, Schmidt number $Sc = \nu/D$, characteristic colony length L and
165 kinematic viscosity ν . Hence $k \propto U_{\text{flow}}^m$, and because near-tissue flow scales with surface wind
166 as $U_{\text{flow}} \propto U^p$, the clearance rate scales as

$$167 \quad k \propto U^{(m \cdot p)}.$$

168 The exponent m encodes the hydrodynamic regime and surface character ($m \approx 0.5$ for smooth
169 surfaces in laminar–transitional flow; $m \approx 0.8–1.0$ for rough, branching morphologies in turbulent
170 flow), while p ranges from $\approx 0.5–1$ where near-surface flow is wave-dominated and only weakly
171 wind-coupled, to ≈ 2 where direct wind stress ($\tau \propto U^2$) drives the near-tissue flow. The composite
172 exponent $m \cdot p$ therefore spans roughly 0.5 to 2. We adopt this range rather than a single value
173 because the morphological coefficient a and the regime exponents vary among coral taxa and
174 habitats, with branching and tabular corals expected to clear reactive oxygen species more
175 efficiently per unit wind than massive or encrusting forms (Nakamura 2010).

176 The exponent (m) reflects hydrodynamic regime and colony morphology, ranging from
177 approximately 0.5 for smooth surfaces in laminar-to-transitional flow to approximately 0.8–1.0 for
178 rough or branching morphologies in turbulent flow. The exponent (p) reflects the coupling between
179 surface winds and near-coral flow, ranging from approximately 0.5–1 where wave-driven
180 circulation dominates and wind coupling is weak, to approximately 2 where direct wind stress ($\tau \propto$
181 U^2) exerts stronger control. The composite exponent ($m \cdot p$) therefore spans roughly 0.5–2. We retain
182 this range rather than a single value because hydrodynamic conditions and colony morphology vary
183 among coral taxa and habitats, with branching and tabular corals expected to experience greater
184 wind-driven enhancement of metabolite and ROS exchange than massive or encrusting forms
185 (Nakamura 2010).

186

187 **Supplementary Note 6. Projected change in mean wind speed over coral reefs** 188 **(CMIP6)**

189 Trade winds are broadly expected to weaken under warming, but how that change is
190 expressed at reef locations is not established. Rather than assume a uniform decline, we
191 characterise the full distribution of projected wind change over reef area and ask two questions:
192 whether mean winds decline or intensify over coral reefs and what the net change is (Q1), and
193 how large the change is, how it is distributed and what it implies for severe-bleaching odds (Q2).

194 ***Data and ensemble construction.***

195 We use monthly mean near-surface wind speed (*sfcwind*, table Amon) from the full
196 available CMIP6 ensemble (Eyring et al. 2016), read directly from the Pangeo Google-Cloud Zarr
197 archive. For each model we compute the change in the climatological mean between 2080–2099
198 and 1995–2014, ΔU , on the model’s native grid, under SSP2-4.5 and SSP5-8.5 (O’Neill et al.
199 2016). One realisation is retained per model (preferring *r1i1p1f1*, otherwise the lowest forcing
200 variant; native grid *gn* preferred, with fallback to *gr/gr1*), yielding 43 models for SSP5-8.5 and 41
201 for SSP2-4.5. Relaxing the earlier *r1i1p1f1*-only selection recovers the f2/f3-forcing models
202 (UKESM1-0-LL, HadGEM3-GC31, the CNRM family, MIROC-ES2L) and the regridded-only

203 models (EC-Earth3, GFDL, IPSL, INM, KIOST). The realisation and grid label retained for every
204 model are listed in Supplementary Table 2.

205 ***Reef sampling.***

206 ΔU is sampled by nearest grid cell at all 63,496 equal-area 5×5 km reef polygons.
207 Because the cells are equal-area, a plain mean or histogram over them is the reef-area-weighted
208 quantity, so no de-clustering correction is needed. One ΔU column per model is written beside the
209 coordinates, with ensemble summaries, in the accompanying data table (Supplementary Code).

210 ***Model independence.***

211 The 43 models derive from 26 institutions (Supplementary Table 2) and fewer
212 independent atmospheric formulations: the CAM/CESM lineage supplies nine models and the
213 UK Met Office UM/HadGEM lineage six, so roughly a third of the ensemble reflects two
214 atmospheric models (Knutti et al. 2013). We therefore report the reef-area-mean both one-model-
215 one-vote and one-centre-one-vote (averaged within institution, then across institutions). The two
216 weightings agree in sign and magnitude (SSP5-8.5: -0.016 versus -0.008 m s^{-1} ; SSP2-4.5:
217 $+0.007$ versus $+0.013$ m s^{-1}), indicating the central estimate is robust to model genealogy.

218 ***Results: distribution and robustness.***

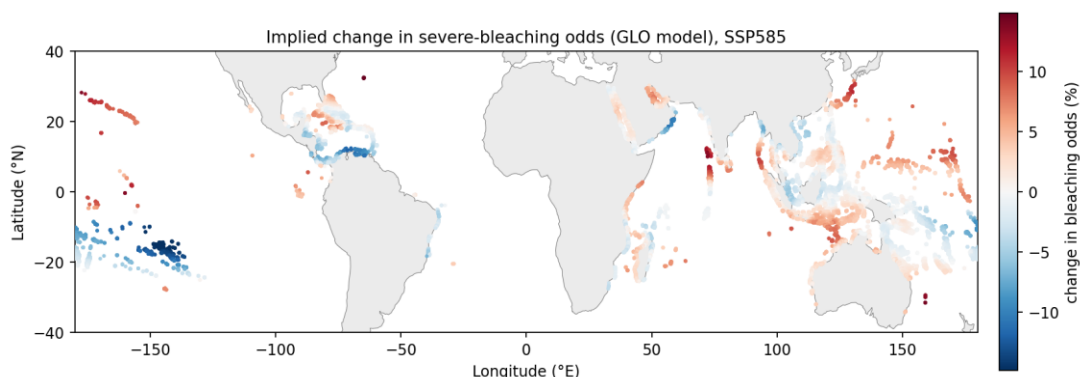
219 Under SSP5-8.5, mean winds weaken over 58.8% of reef area, but the net change is small
220 (area-mean ΔU -0.016 m s^{-1} ; area-weighted median -0.020 ; 5th–95th percentile -0.225 to
221 $+0.191$ m s^{-1}) and of limited robustness: at least 66% of models agree on a decline over only
222 26.4% of reef area, and at least 80% agree on the sign over only 19.4%. A two-thirds threshold
223 (66%) is commonly used as an indicator of moderate model agreement in CMIP ensemble
224 analyses. Under SSP2-4.5 the net change is indistinguishable from zero (area-weighted median
225 -0.002 m s^{-1} ; 51.1% of area declining). The small area-mean reflects cancellation of sizeable
226 regional declines and increases rather than a consensus of no change, so the decisive diagnostic is
227 the sign-agreement fraction, not the mean. The higher-emissions scenario shows slightly more
228 reef-wind weakening than the moderate one, consistent with a stronger forced slackening of the
229 trade winds. We note that CMIP6 models share known biases in the simulation of tropical
230 circulation, including the projected weakening of the Pacific Walker cell, so these wind
231 projections carry structural as well as scenario uncertainty; this reinforces our treatment of the net
232 change as a low-confidence, spatially variable tendency rather than a robust trend.

233 ***Translation to severe-bleaching odds.***

234 Per-reef ΔU is converted to a change in severe-bleaching odds using the GLO within-
235 region 6-month wind coefficient (odds ratio ≈ 0.70 per s.d.; s.d. ≈ 1.2 m s^{-1} ; van Woesik &
236 Kratochwill 2022), the conceptual match to a sustained multidecadal change in climatological
237 mean wind. Because the fitted sensitivity derives from the 6-month antecedent wind whereas the
238 projected change is in the multidecadal climatological mean, this translation applies the
239 antecedent coefficient as a conceptual proxy rather than a like-for-like predictor; given that the
240 long-term mean wind is itself only weakly related to severity in our data, the projected odds
241 changes should be read as indicative of direction and relative magnitude rather than as calibrated
242 forecasts. At the area-mean the implied change is $+0.6\%$ (SSP5-8.5) and -0.2% (SSP2-4.5); at the
243 most strongly wind-declining reefs it reaches $+19\%$ (SSP5-8.5; $\Delta U \approx -0.58$ m s^{-1}) and $+8.5\%$
244 (SSP2-4.5). The steeper SAF 12-month coefficient (odds ratio ≈ 0.45 per s.d.; Safaie et al. 2018)
245 gives roughly 2–2.5 \times these values — up to $\approx +47\%$ (SSP5-8.5) and $+20\%$ (SSP2-4.5) at the
246 extreme — and is reported as a sensitivity bracket rather than a co-equal map, because its event-

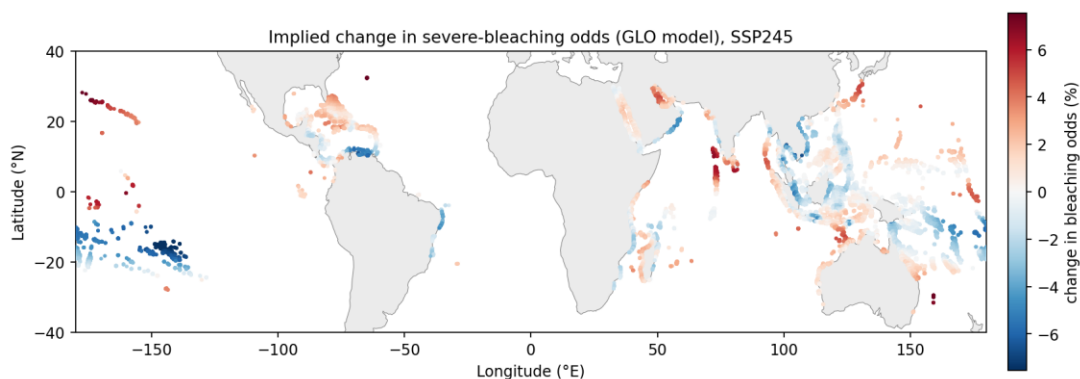
247 window provenance ($n = 81$) makes a multidecadal climatological projection an over-extension if
 248 presented as an independent estimate. The change in severe-bleaching odds is mapped in main-
 249 text Fig. 6 (GLO model); Supplementary Figure 2 shows both scenarios and the ΔU distribution.
 250 For each reef the odds multiplier is the per-standard-deviation odds ratio raised to the
 251 standardized wind change, $(OR)^{(\Delta U/\sigma)}$, with σ the across-reef standard deviation of background
 252 wind; for completeness, the SAF area-mean change is $\approx +1.5\%$ (SSP5-8.5), with a per-reef 5th–
 253 95th-percentile range of roughly -12% to $+16\%$.

254 **a GLO odds change, SSP5-8.5**



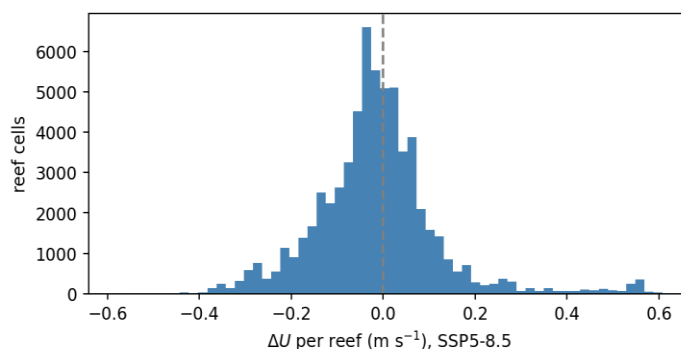
255

256 **b GLO odds change, SSP2-4.5**



257

258 **c Distribution of per-reef ΔU , SSP5-8.5**



259

260 **Supplementary Figure 2. Implied change in severe-bleaching odds and the ΔU distribution.** (a,b)
 261 Per-reef change in severe-bleaching odds from projected ΔU using the GLO 6-month wind
 262 coefficient, for SSP5-8.5 and SSP2-4.5; red, higher odds (weakening winds); blue, lower odds
 263 (strengthening winds); continental outlines from Natural Earth. (c) Distribution of ensemble-

264 mean ΔU across all 63,496 reef cells under SSP5-8.5, with the mode just below zero and a
 265 heavier negative tail. The SAF coefficient gives roughly 2–2.5× the odds amplitude of GLO and
 266 is reported as a sensitivity bracket above.

267 **Supplementary Table 2.** CMIP6 models, realisations and grids used in the wind-projection
 268 analysis (SSP5-8.5).

source_id	institution_id	member_id	grid
ACCESS-CM2	CSIRO-ARCCSS	r1i1p1f1	gn
ACCESS-ESM1-5	CSIRO	r1i1p1f1	gn
AWI-CM-1-1-MR	AWI	r1i1p1f1	gn
BCC-CSM2-MR	BCC	r1i1p1f1	gn
CAMS-CSM1-0	CAMS	r1i1p1f1	gn
CAS-ESM2-0	CAS	r1i1p1f1	gn
CESM2	NCAR	r4i1p1f1	gn
CESM2-WACCM	NCAR	r1i1p1f1	gn
CMCC-CM2-SR5	CMCC	r1i1p1f1	gn
CMCC-ESM2	CMCC	r1i1p1f1	gn
CNRM-CM6-1	CNRM-CERFACS	r1i1p1f2	gr
CNRM-CM6-1-HR	CNRM-CERFACS	r1i1p1f2	gr
CNRM-ESM2-1	CNRM-CERFACS	r1i1p1f2	gr
CanESM5	CCCma	r1i1p1f1	gn
CanESM5-CanOE	CCCma	r1i1p2f1	gn
E3SM-1-1	E3SM-Project	r1i1p1f1	gr
EC-Earth3	EC-Earth-Consortium	r1i1p1f1	gr
EC-Earth3-CC	EC-Earth-Consortium	r1i1p1f1	gr
EC-Earth3-Veg	EC-Earth-Consortium	r1i1p1f1	gr
EC-Earth3-Veg-LR	EC-Earth-Consortium	r1i1p1f1	gr

FGOALS-f3-L	CAS	rlilp1f1	gr
FGOALS-g3	CAS	rlilp1f1	gn
FIO-ESM-2-0	FIO-QLNM	rlilp1f1	gn
GFDL-CM4	NOAA-GFDL	rlilp1f1	gr1
GFDL-ESM4	NOAA-GFDL	rlilp1f1	gr1
GISS-E2-1-G	NASA-GISS	rlilp3f1	gn
HadGEM3-GC31-LL	MOHC	rlilp1f3	gn
HadGEM3-GC31-MM	MOHC	rlilp1f3	gn
IITM-ESM	CCCR-IITM	rlilp1f1	gn
INM-CM4-8	INM	rlilp1f1	gr1
INM-CM5-0	INM	rlilp1f1	gr1
IPSL-CM6A-LR	IPSL	rlilp1f1	gr
KACE-1-0-G	NIMS-KMA	rlilp1f1	gr
KIOST-ESM	KIOST	rlilp1f1	gr1
MIROC-ES2L	MIROC	rlilp1f2	gn
MIROC6	MIROC	rlilp1f1	gn
MPI-ESM1-2-HR	MPI-M	rlilp1f1	gn
MPI-ESM1-2-LR	MPI-M	rlilp1f1	gn
MRI-ESM2-0	MRI	rlilp1f1	gn
NorESM2-LM	NCC	rlilp1f1	gn
NorESM2-MM	NCC	rlilp1f1	gn
TaiESM1	AS-RCEC	rlilp1f1	gn
UKESM1-0-LL	MOHC	rlilp1f2	gn

269 Total: 43 models from 26 institutions. SSP2-4.5 uses the same set minus ACCESS-ESM1-5 and
 270 HadGEM3-GC31-MM (41 models). Datasets were read from the Pangeo CMIP6 Zarr archive
 271 (gs://cmip6/CMIP6/...).

272 **Supplementary Note 7. Robustness of the wind association.**

273 The global analysis retains one bleaching record per 5×5 km reef site (sites ≥ 5 km
 274 apart); the 0.25° grid is used only to attach the gridded SST and wind fields, so several sites can
 275 fall within one 0.25° wind/SST cell (275 of 835 occupied cells contain ≥ 2 sites, which therefore
 276 share identical gridded predictors). To confirm that the wind association is not an artefact of this
 277 shared structure, we refitted the ordinal model (i) with a cluster bootstrap that resamples whole
 278 0.25° cells and (ii) after collapsing to a single (earliest) record per 0.25° cell. The 6-month
 279 antecedent-wind odds ratio is essentially unchanged under both (Supplementary Table 3). We
 280 additionally compared antecedent windows: the protective association is strongest for the 6-
 281 month mean, weaker for the 12-month mean, and absent for the long-term 1993–2020 mean,
 282 consistent with a seasonal-to-annual rather than decadal mechanism.

283 **Supplementary Table 3. Robustness of the GLO 6-month-wind odds ratio.**

Model variant	<i>n</i>	Wind OR (per s.d.)	95% CI
Pooled OLR, all sites (reported)	1,190	0.70	0.61–0.80
Cluster bootstrap by 0.25° cell	1,190	0.70	0.58–0.80
One record per 0.25° cell (earliest)	833	0.67	0.57–0.79

284 *Wind-window comparison (same controls; all odds ratios per s.d.):* 6-month OR =
 285 0.70 ($P < 10^{-6}$); 12-month OR = 0.85 ($P = 0.02$); long-term (1993–2020) OR =
 286 1.08 ($P = 0.36$).

287

288 **Supplementary References**

289 Cited across Supplementary Notes 1–7, in author–year style consistent with the notes. Individual
 290 CMIP6 dataset DOIs can be exported from the WCRP CMIP6 citation service.

291 Bell, A. & Jones, K. Explaining fixed effects: random effects modeling of time-series cross-
 292 sectional and panel data. *Polit. Sci. Res. Methods* 3, 133–153 (2015).

293 de Boyer Montégut, C., Madec, G., Fischer, A. S., Lazar, A. & Iudicone, D. Mixed layer depth
 294 over the global ocean: an examination of profile data and a profile-based climatology. *J.*
 295 *Geophys. Res.* 109, C12003 (2004).

296 Emanuel, K. Increasing destructiveness of tropical cyclones over the past 30 years. *Nature* 436,
297 686–688 (2005).

298 Eyring, V. *et al.* Overview of the Coupled Model Intercomparison Project Phase 6 (CMIP6)
299 experimental design and organization. *Geosci. Model Dev.* 9, 1937–1958 (2016).

300 Grömping, U. Estimators of relative importance in linear regression based on variance
301 decomposition. *Am. Stat.* 61, 139–147 (2007).

302 Hoffert, M. I., Callegari, A. J. & Hsieh, C.-T. A box-diffusion carbon-cycle model with
303 upwelling, polar bottom-water formation and a marine biosphere. In *Carbon Cycle Modelling*
304 (*SCOPE 16*) (ed. Bolin, B.) 287–305 (Wiley, 1981).

305 Holland, G. J. An analytic model of the wind and pressure profiles in hurricanes. *Mon. Weather*
306 *Rev.* 108, 1212–1218 (1980).

307 Itoh, S. *et al.* Vertical turbulent diffusivity across the Pacific pycnocline. (2021).

308 Knapp, K. R., Kruk, M. C., Levinson, D. H., Diamond, H. J. & Neumann, C. J. The International
309 Best Track Archive for Climate Stewardship (IBTrACS). *Bull. Am. Meteorol. Soc.* 91, 363–
310 376 (2010).

311 Knutti, R., Masson, D. & Gettelman, A. Climate model genealogy: generation CMIP5 and how
312 we got there. *Geophys. Res. Lett.* 40, 1194–1199 (2013).

313 Lavigne, H. & Gattuso, J.-P. seacarb: seawater carbonate chemistry with R. R package (2012).

314 McFadden, D. Conditional logit analysis of qualitative choice behavior. In *Frontiers in*
315 *Econometrics* (ed. Zarembka, P.) 105–142 (Academic Press, 1974).

316 Mundlak, Y. On the pooling of time series and cross section data. *Econometrica* 46, 69–85
317 (1978).

318 Nakamura, T. Importance of water flow on the physiological responses of reef-building corals.
319 *Galaxea* 12, 1–14 (2010).

320 O’Neill, B. C. *et al.* The Scenario Model Intercomparison Project (ScenarioMIP) for CMIP6.
321 *Geosci. Model Dev.* 9, 3461–3482 (2016).

322 Safaie, A. *et al.* High frequency temperature variability reduces the risk of coral bleaching. *Nat.*
323 *Commun.* 9, 1671 (2018).

324 Shapley, L. S. A value for n-person games. In *Contributions to the Theory of Games II* (eds
325 Kuhn, H. W. & Tucker, A. W.) 307–317 (Princeton Univ. Press, 1953).

326 Spalding, M. D. *et al.* Marine ecoregions of the world: a bioregionalization of coastal and shelf
327 areas. *BioScience* 57, 573–583 (2007).

328 van Woesik, R. & Kratochwill, C. A global coral-bleaching database, 1980–2020. *Sci. Data* 9, 20
329 (2022).

330 Wallcraft, A. J. *et al.* Comparisons of monthly mean 10-m wind speed from satellite and NWP
331 products over the global ocean. *J. Geophys. Res.* 114, D16109 (2009).

332 Wanninkhof, R. Relationship between wind speed and gas exchange over the ocean revisited.
333 *Limnol. Oceanogr. Methods* 12, 351–362 (2014).

334 Weiss, R. F. Carbon dioxide in water and seawater: the solubility of a non-ideal gas. *Mar. Chem.*
335 2, 203–215 (1974).

336 Natural Earth. Free vector and raster map data, naturalearthdata.com (110 m land/coastline).